



Crystal facet-dependent frustrated Lewis pairs on dual-metal hydroxide for photocatalytic CO₂ reduction

Weining Zhang^{a,b,1}, Zhenhua Yang^{a,1}, Hailian Wang^{a,1}, Lei Lu^{a,b}, Depei Liu^{a,b}, Taozhu Li^a, Shicheng Yan^{a,*}, Hao Qin^{a,*}, Tao Yu^{a,b,**}, Zhigang Zou^{a,b}

^a Eco-materials and Renewable Energy Research Center (ERERC), Collaborative Innovation Center of Advanced Microstructures, College of Engineering and Applied Sciences, Nanjing University, No. 22 Hankou Road, Nanjing, Jiangsu 210093, PR China

^b Jiangsu Key Laboratory for Nano Technology, National Laboratory of Solid State Microstructures, School of Physics, Nanjing University, No. 22 Hankou Road, Nanjing, Jiangsu 210093, PR China

ARTICLE INFO

Keywords:

Frustrated Lewis pairs
Molecule activation
Photocatalysis
CO₂ reduction

ABSTRACT

CO₂ activation is a vital knot for CO₂-mediated energy conversion and storage. Frustrated Lewis pairs (FLPs) are well confirmed to be highly efficient in CO₂ activation. Here, we synthesized the single-crystal ZnSn(OH)₆ cube with exposed (100) facet (Sc) and ZnSn(OH)₆ octahedra with exposed (111) facet (So) and created FLPs with different acid-base distance on these exposed facets by vacuum irradiation, resulting from the light instability of terminal hydroxyls. Our results demonstrated that the FLPs with short acid-base distance on So are more efficient activation centers due to the strong orbital interactions, well exemplifying that shortening the Lewis acid-base distance is a potential route to develop highly efficient FLPs catalysts. In addition, as an initial attempt, the combination effects between facet junction separating charges and FLPs activating molecules were proposed to accelerate CO₂ reduction. Our findings may provide new insights into designing photocatalysts with highly catalytic performances.

1. Introduction

Global warming has become one of the serious problems all over the world with the increase of carbon dioxide (CO₂) emission [1–3]. Under this circumstance, photocatalytic reduction of CO₂ is one of the potential technologies to convert and store solar energy into high value-added chemical fuels [4–6]. However, the higher activation energies of CO₂ molecules with the stable C=O bonds greatly limit the conversion efficiency for photocatalytic CO₂ reduction. It was found that the higher CO₂ conversion efficiency could be achieved by constructing frustrated Lewis pairs (FLPs) [7–12]. In terms of Lewis acid-base theory, Stephan et al. first pointed out the catalytic application of FLPs in 2006 [13]. Specifically, an active region instead of coordination bonds could be formed due to the larger steric hindrance between Lewis acid with an unoccupied orbital and Lewis base with lone pair electrons. When small molecules enter the active region of FLPs, the bonding and anti-bonding orbitals of small molecules would interact with the Lewis acid and Lewis

base, respectively, resulting the polarization and heterolysis of small molecules, thus the reaction kinetics would be promoted during the catalytic process. In recent years, a series of FLPs studies have demonstrated that all-solid FLPs catalysts is more beneficial to the catalytic reactions due to the well recyclability and stability compared to homogeneous FLPs catalysts [14,15]. In 2015, Ozin's group found that the FLPs could be successfully established between unsaturated In³⁺ (Lewis acid) and its adjacent In-OH (Lewis base) on surface of cubic In₂O_{3-x}(OH)_y through the thermal dehydration of In(OH)₃. The catalytic efficiency over CO₂ + H₂ → CO + H₂O has been greatly improved mainly because of the effective activation of H₂ molecules by FLPs [16]. In 2019, it was reported that another types of indium oxides, rhombohedral In₂O_{3-x}(OH)_y, designed by polymorph selection strategy, could achieve higher performance when CO₂ catalyzed to CH₃OH and CO mainly due to the enhanced adsorption strength for intermediates and the increased heterolysis ability for H₂ over FLPs [17]. Recently, we found that the hydroxides with light-unstable terminal hydroxyls, such

* Corresponding authors.

** Corresponding author at: Eco-materials and Renewable Energy Research Center (ERERC), Collaborative Innovation Center of Advanced Microstructures, College of Engineering and Applied Sciences, Nanjing University, No. 22 Hankou Road, Nanjing, Jiangsu 210093, PR China.

E-mail addresses: yscfei@nju.edu.cn (S. Yan), qh_0302@163.com (H. Qin), yutao@nju.edu.cn (T. Yu).

¹ These authors contributed equally to this work.

as $\text{ZnSn}(\text{OH})_6$, are a kind of potential materials to construct FLPs on inorganic materials [18]. However, the factors to affect the activity of FLPs on inorganic materials keep unclear still.

Here, selectively photocorroding of the light-unstable terminal hydroxyls by using the vacuum irradiation, we created the FLPs with different acid-base distance on $\text{ZnSn}(\text{OH})_6$ cube with exposed (100) facet (Sc) and $\text{ZnSn}(\text{OH})_6$ octahedra with exposed (111) facet (So). The FLPs with short acid-base distance on So are more efficient in capturing and activating of CO_2 molecules due to the strong orbital interactions. This fact suggested that shortening the Lewis acid-base distance is a potential route to develop highly efficient FLPs catalysts. In addition, as an initial attempt, we explored the combination effects between facet junction separating charges and FLPs activating molecules to accelerate CO_2 reduction. Our findings may provide new insights into designing photocatalysts with highly catalytic performances.

2. Experimental section

2.1. Preparation of $\text{ZnSn}(\text{OH})_6$ single crystals

Zinc acetate monohydrate [$\text{Zn}(\text{CH}_3\text{COO})_2 \cdot \text{H}_2\text{O}$], tin(IV) chloride tetrahydrate ($\text{SnCl}_4 \cdot 4\text{H}_2\text{O}$), and sodium hydroxide (NaOH) were purchased by Sinopharm chemical reagent Co., Ltd (Shanghai, China). All the chemicals were received from commercial sources of analytical grade without any purification. The $\text{ZnSn}(\text{OH})_6$ with different morphologies were prepared by a facile low-temperature hydrothermal method. Typically, the mixed solution of $\text{SnCl}_4 \cdot 4\text{H}_2\text{O}$ (0.5 M, 12.5 mL) and $\text{Zn}(\text{CH}_3\text{COO})_2 \cdot \text{H}_2\text{O}$ (0.5 M, 12.5 mL) was stirred in 100 mL Teflon autoclave until the mixture becomes transparent. Then NaOH solution (1.625 M, 25 mL) was introduced into the mixed solution at a constant rate, followed by hydrothermal treatment at 100 °C for 8 h to produce the single-crystal cubic $\text{ZnSn}(\text{OH})_6$ particles (denoted as Sc). The single-crystal cuboctahedra and octahedra $\text{ZnSn}(\text{OH})_6$ particles (denoted as Sco and So, respectively) were achieved by adjusting the concentration of NaOH solution (2.375 M, 25 mL for Sco and 3.0 M, 25 mL for So).

2.2. CO_2 photoreduction

The photocatalytic reduction of CO_2 was tested in a glass reactor. The catalysts (100 mg) were dispersed uniformly on the glass reactor with an area of 4.2 cm^2 and the volume of the reactor was about 230 mL. The reaction chamber was vacuum-treated several times, and then high-purity CO_2 (99.999%) was introduced to reach an atmospheric pressure. A 300 W Xenon lamp was served as the light source (nominal power 50 W, irradiation diameter 2.5 cm, light intensity 1.02 kW m^{-2}) with an irradiation perpendicular to surface of samples. Prior to irradiation, the as-prepared photocatalyst was maintained in dark atmosphere for 12 h to reach the adsorption-desorption equilibrium of CO_2 . During the reaction, 1 mL gas was extracted by sampling needle from the chamber at given intervals for subsequent CO and CH_4 concentration measurement by gas chromatography (GC-2014, Shimadzu Corp., Japan).

2.3. Characterizations

The crystallographic phase of the samples was determined by powder X-ray diffraction (XRD, Rigaku Ultima III, Japan) operated with Cu K_α radiation (40 kV and 40 mA). The morphology of the samples was observed by FEI NOVA Nano scanning electron microscope (SEM) 230. Fourier transform infrared spectroscopy (FT-IR) was acquired on a Nicolet Nexus 870 infrared spectrometer (Nicolet, USA) with 2 cm^{-1} resolution. The X-ray photoelectron spectroscopy (XPS) data were received through a PHI5000 Versa Probe X-ray photoelectron spectrometer (Al K_α radiation, $h\nu = 1486.6$ eV). The binding energy was referenced to the $\text{C}1s$ line at 284.6 eV. Electron paramagnetic resonance (EPR) spectra were recorded at room temperature using an electron

paramagnetic resonance spectrometer (model EMX-10/12 X-band, Bruker, Germany) operating at a frequency of 9.383 GHz. A powdered 50 mg sample was placed in a quartz tube and four scans were collected per spectrum at a microwave power of 10 mW. The g factor was calculated by $g = h\nu/\beta H$, where h is the Planck's constant, ν is the microwave frequency, β is the Bohr magneton, and H is the magnetic field at which resonance occurred. The ultraviolet-visible (UV-vis) diffuse reflectance spectra were recorded using a UV-vis spectrophotometer (UV-2550, Shimadzu, Japan) at room temperature and transformed into the absorption spectra by the Kubelka-Munk relationship. The Mott-Schottky measurements were performed using an electrochemical analyzer (CHI660E, Chenhua, China) with a homemade standard three-electrode cell. The working electrodes were prepared by a drop-coating method. Specially, the sample suspensions were coated onto indium-tin oxide (ITO) glass (1 cm^2) surface and then dried at 80 °C for 2 h in vacuum oven.

2.4. Theoretical calculations

Density functional theory (DFT) calculations were simulated by the projected augmented wave (PAW) method in the Vienna ab initio simulation package (VASP) [19,20]. The exchange-correlation energy was described by the Perdew, Burke, and Ernzerhof (PBE) function with the generalized gradient approximation (GGA) method [21]. The kinetic energy cutoff for a plane wave basis set was 400 eV. We applied Monkhorst Pack mesh k-points of (3 × 3 × 1) for (100) and (111) surfaces of Sc and So, with convergence of 0.1 meV for total electronic energy and 0.05 eV/Å for remaining total force.

3. Results and Discussion

3.1. $\text{ZnSn}(\text{OH})_6$ single crystals with different exposed facets

The structures and morphologies of the as-prepared $\text{ZnSn}(\text{OH})_6$ were examined with X-ray diffraction (XRD) and scanning electron microscopy (SEM). As shown in Fig. 1a, the XRD patterns of these samples displayed the same diffraction peaks, well assigning to the single-phase $\text{ZnSn}(\text{OH})_6$ with a cubic structure (JCPDS card No. 20-1455). The SEM images demonstrated that the monodispersed single-crystal $\text{ZnSn}(\text{OH})_6$ cubes (denoted as Sc) with particle size of about 2 μm formed in low-concentration NaOH solution (Fig. 1b). Increasing the concentration of NaOH will produce the single-crystal $\text{ZnSn}(\text{OH})_6$ octahedrons (denoted as So) with the similar particle size to Sc (Fig. 1c). Considering the cubic crystal structure of $\text{ZnSn}(\text{OH})_6$, the single-crystal cube and octahedron would expose the (100) and (111) facets, respectively. The formations of Sc and So with different exposed facets were mainly attributed to the different growth rates of (100) and (111) facets under different OH^- concentrations [22-24]. Fourier transform infrared (FTIR) spectra of both Sc and So exhibited the similar bands (Fig. 1d), suggesting that the same groups existed in Sc and So. Bands at 539 and 656 cm^{-1} were respectively assigned to the stretching vibrations of Sn-O or M-O-M bonds in Sc and So [25], and the band at 1170 cm^{-1} could be corresponded to the bending vibrations of Sn-OH bonds. The bands at 2296 cm^{-1} and 773 cm^{-1} were designated to the surface adsorbed CO_2 and H_2O - H_2O hydrogen bonding, respectively [26]. In addition, the bands at 3086-3229 cm^{-1} and 1639 cm^{-1} resulted from the stretching vibration and bending vibration of O-H bonds, respectively [27]. Moreover, the slight difference in vibrations of O-H bonds of Sc and So indicated their different atomic arrangement of M-OH or M-OH-M. The structure optimization by density functional theory (DFT) verified that the stable (100) facet is comprising of bridging hydroxyl isolated Zn-OH and Sn-OH terminal hydroxyls (Fig. 1e). However, the stable (111) facet exhibited the Sn-centered $\text{Sn}(\text{OH})_6$ octahedrons with three terminal hydroxyls (Fig. 1f). This means that the (100) facet tends to expose bridging hydroxyl and terminal hydroxyl. The (111) facet likes to expose the Sn-bonding three terminal hydroxyls. The different atomic

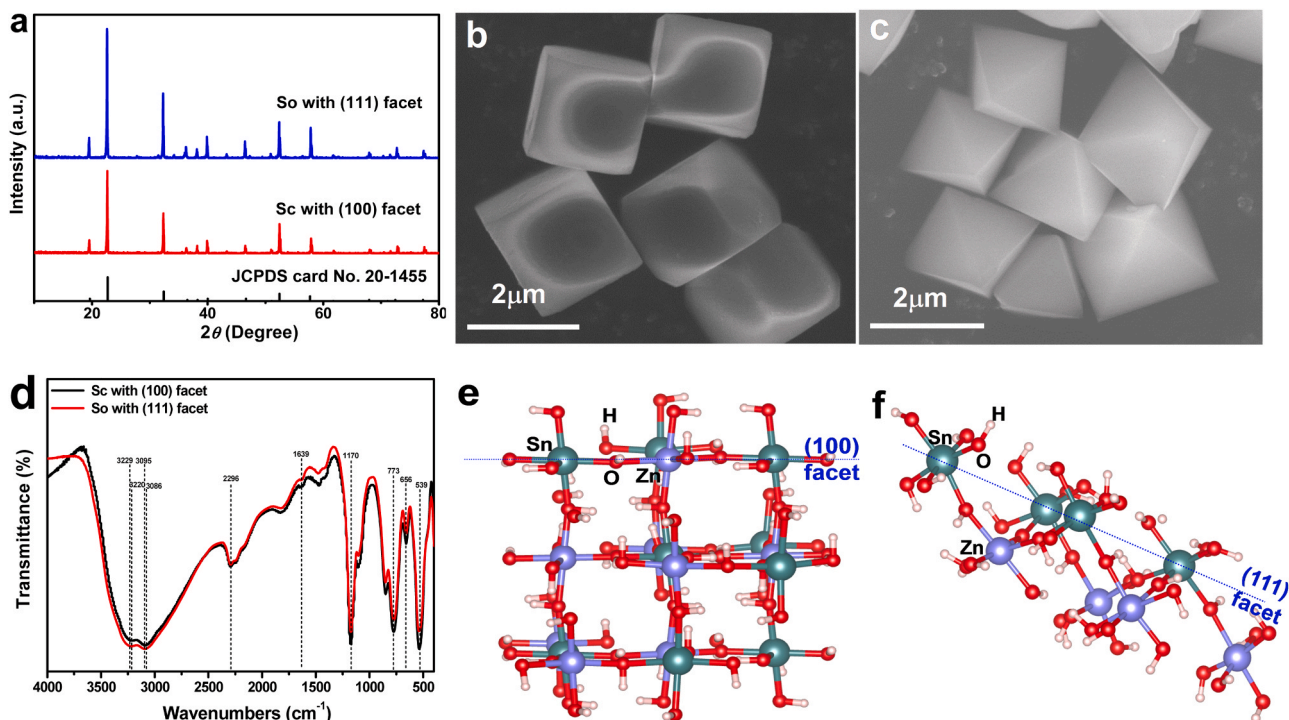


Fig. 1. Crystallographic structure and morphology of $\text{ZnSn}(\text{OH})_6$ single crystal. (a) XRD patterns. (b) and (c) SEM images of Sc with (100) facet and So with (111) facet. (d) FTIR spectra of Sc with (100) facet and So with (111) facet. (e) and (f) The surface atomic arrangement for Sc with (100) facet and So with (111) facet.

arrangement for hydroxyl groups may induce the slight difference in FTIR signals of hydroxyl groups for $\text{ZnSn}(\text{OH})_6$ with exposed different facets.

3.2. FLPs generation on surface of Sc and So

Next, we checked the FLPs generation on surface of Sc and So by vacuum pre-irradiation. According to the comparison of catalytic properties among the samples with different pre-irradiation time

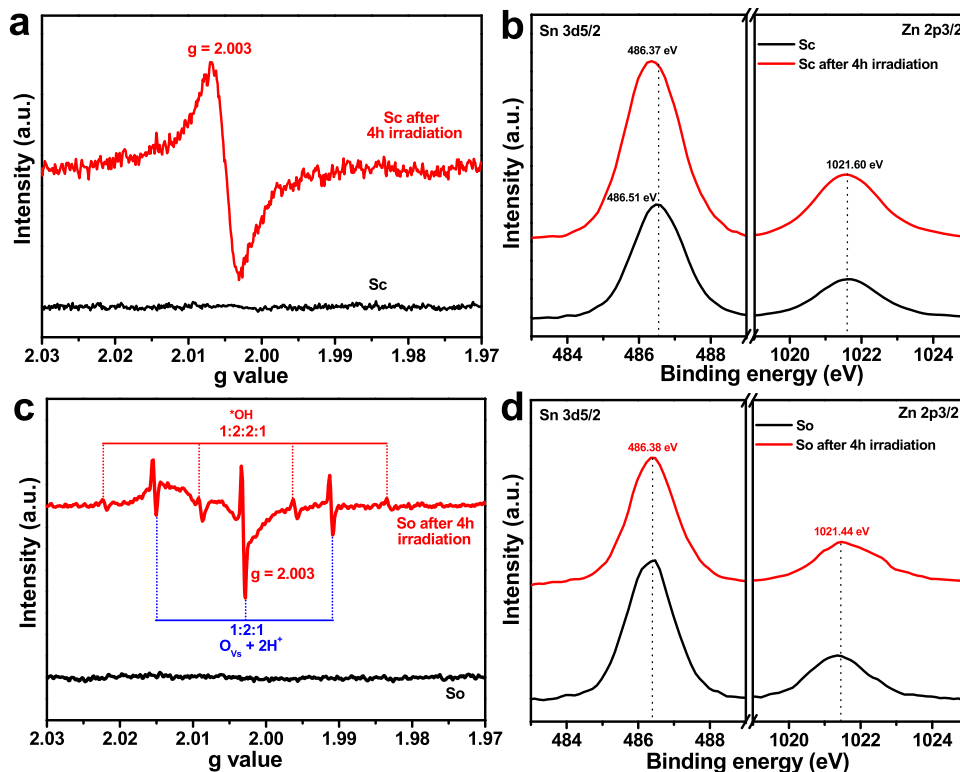


Fig. 2. EPR and XPS spectra for $\text{ZnSn}(\text{OH})_6$ materials with different specific exposed facet before and after 4 h vacuum irradiation. (a) EPR and (b) XPS spectra of Sc. (c) EPR and (d) XPS spectra of So.

(Fig. S1, Supporting Information), the vacuum pre-irradiation 4 h sample with the best catalytic activity is selected to explore the difference of FLPs generation between Sc and So. After pre-irradiation for 4 h, a typical EPR signal of oxygen vacancy (O_V s) at $g = 2.003$ was observed for Sc sample (Fig. 2a), indicating that surficial terminal hydroxyls may be oxidized due to the photocorrosion during pre-irradiation process [28]. As described in Fig. 1e, on the (100) facet, there are two kinds of terminal hydroxyls, Zn-OH and Sn-OH, and a bridging hydroxyl Zn-OH-Sn. The lattice bridging hydroxyls would be more stable than the terminal hydroxyls due to the strong lattice constraint. Therefore, the irradiation likes to preferentially corrode the relatively unstable terminal hydroxyls, Zn-OH or Sn-OH, to generate O_V s as a result of hole oxidation via a reaction of $2OH^- + h^+ = H_2 + O_2$. After 4 h vacuum irradiation, about 0.14 eV decrease in binding energy of Sn 3d5/2 was observed, while the binding energy of Zn 2p3/2 kept constant (Fig. 2b). This evidence suggested that the six-coordinated Sn^{4+} center in $Sn(OH)_6$ octahedra tends to gain electrons due to the bigger electronegativity for Sn (1.706) than Zn (1.336) [29]. However, the low-valence $Sn^{\delta+}$ ($\delta < 4$) exhibited sharply decreased electronegativity [29], such as 1.181 for Sn^{2+} , thus inducing the lower stability for Sn-OH than Zn-OH bonds. The nearly similar FTIR spectra were observed before and after 4 h vacuum irradiation (Fig. S2, Supporting Information), suggesting that the photocorrosion occurs at the surface of samples. Accordingly, we believe that the O_V s generation resulted from the photocorrosion of Sn-OH by hole oxidation. The light-stable Zn-OH as Lewis base and adjacent unsaturated $Sn^{\delta+}$ as Lewis acid are more likely to form FLPs.

For So sample, the stable terminal facet exposed Sn-OH arrangement and the Zn-OH located at sublattice. The vacuum irradiation gives rise to exclusively a 1:2:2:1 quartet signal in the EPR spectrum, is typical characteristic of $\bullet OH$ radicals (Fig. 2c) [30]. In addition, a 1:2:1 EPR signal centered at $g = 2.003$ was assigned to the super-hyperfine splitting of two proton trapped by O_V s [31,32]. On the (111) facet, the exposed Sn-centered $Sn(OH)_6$ octahedron has three terminal hydroxyls. Under irradiation, the relatively unstable terminal hydroxyl has an opportunity to be corroded by hole to form O_V s, which is able to construct FLPs with the adjacent stable -OH bonding to the same Sn center. The distance between Lewis acid (O_V s) and Lewis base (-OH) for such a FLPs on the Sn site is small to be 0.207 nm, closed to the length of Sn-O, thus exhibiting the strong capturing ability of protons. The $\bullet OH$ radicals may result from the O_V s generation by hole oxidation of Sn-OH to $\bullet OH$, probably implying that the Sn-OH on (111) facet is relatively stable. Indeed, the quantitative EPR analysis indicated that the concentration of O_V s in So (7.98×10^{13} spin/g) is about three orders of magnitude lower than that in Sc (1.36×10^{16} spin/g), confirming the higher stability of Sn-OH on (111) facet. The no obvious changes in XPS binding energies of Zn 2p and Sn 3d for So before and after irradiation were observed (Fig. 2d), further verified that the low-concentration O_V s formed on (111) facet.

3.3. CO_2 reduction on FLPs of $ZnSn(OH)_6$

As shown in Fig. 3a, on (100) facet, the typical distance between O_V s Lewis acid and Zn-OH Lewis base is about 0.488 nm. However, the FLP distance on (111) facet is 0.207 nm. The smaller FLP distance means a strong capturing ability of molecules. It is interesting to check the CO_2 reduction on FLPs with different distance between Lewis acid and base centers. The CO_2 reduction experiment was carried out in high-purity CO_2 without addition of H_2O . Directly illuminating the materials without vacuum pre-irradiation will produce CO as main product and CH_4 as minor product. The average generation rates of CO and CH_4 are 0.121 and $0.034 \mu mol g_{cat}^{-1} h^{-1}$ for Sc and 0.126 and $0.032 \mu mol g_{cat}^{-1} h^{-1}$ for So, respectively (Fig. 3b, Fig. S3, Supporting Information). In this situation, the CO_2 adsorption may stabilize the hydroxyls on Sc and So. Therefore, we believe that the CO and CH_4 generation over Sc and So exhibited their inherent catalytic activities of CO_2 reduction. And under the condition without water addition the CO_2 reduction would result from the reaction between CO_2 and adsorbed H_2O on catalysts. After creating FLPs by 4 h vacuum irradiation, the generation rate of CO and CH_4 was increased up to 7.31 and $0.68 \mu mol g_{cat}^{-1} h^{-1}$ for Sc and 3.27 and $0.42 \mu mol g_{cat}^{-1} h^{-1}$ for So, respectively (Fig. 3c). During the vacuum irradiation, the light-unstable hydroxyls were oxidized by hole to form O_V s with H_2 generation via reaction of $2OH^- = H_2 + O_2$. When CO_2 was introduced into reaction system, the CO generation follows a reaction of $CO_2 + H_2 \rightarrow CO + H_2O$. For the So, the hyperfine splitting EPR signal for protons trapped at O_V s clearly suggested that during the CO_2 reduction the H_2 was first captured and heterolytically cleaved by FLPs (Fig. 2c). Although the concentration of FLPs is about 1000 times higher for Sc than So, the CO generation rate is only about 2.2 times higher for Sc than So. This fact means that the FLPs on So is more effective for activation of CO_2 and H_2 .

In addition, the CO_2 reduction experiment was performed in high-purity CO_2 with addition of H_2O to investigate the effects of H_2O in catalytic process. The activity of So-pre-irradiation 4 h sample with H_2O displays a slight decreasing trend compared to So-pre-irradiation 4 h sample without H_2O (Fig. S4, Supporting Information), demonstrating that the presence of H_2O has no facilitating effects for photocatalytic CO_2 reduction. And the slight decrease in catalytic activity after addition of H_2O perhaps due to the active sites are blocked by H_2O molecules to some extent. As a result, the CO_2 reduction performance present a decreasing tendency. As the FLPs on So-pre-irradiation 4 h sample have the stronger activation ability, thus the So-pre-irradiation 4 h sample is selected to investigate the stability of catalyst. As shown in Fig. S5, the morphology and crystal structure of the used So-pre-irradiation 4 h sample have no obvious variation compared to the fresh one, indicating the well stability of the So-pre-irradiation 4 h sample after reaction. Furthermore, the recycle experiment is also carried out in high-purity CO_2 without addition of H_2O . The activity of So-pre-irradiation 4 h sample present slight decrease from ca. $28.8 \mu mol g_{cat}^{-1}$ to ca.

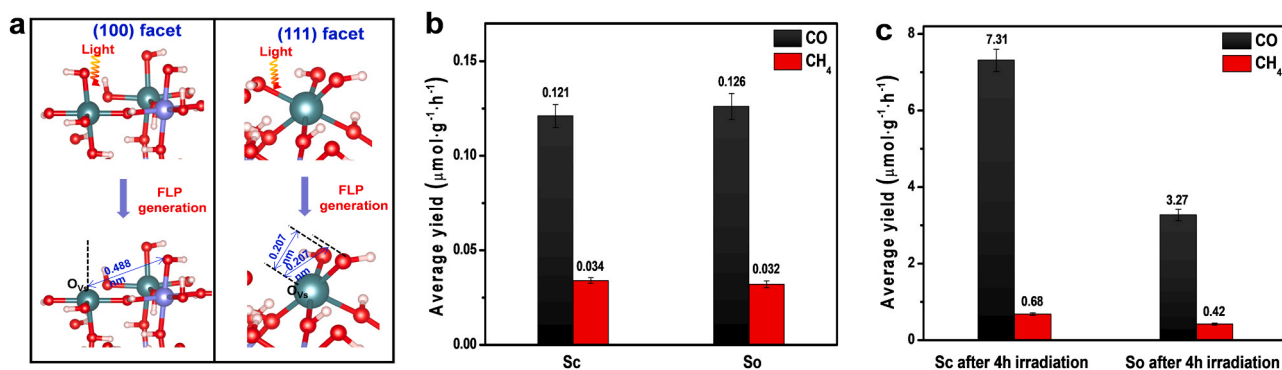


Fig. 3. (a) The FLPs generation on (100) and (111) facets by photocorrosion. (b) The generation rate of CO and CH_4 over So and Sc. (c) The generation rate of CO and CH_4 over So and Sc with 4 h vacuum irradiation.

20.0 $\mu\text{mol g}_{\text{cat}}^{-1}$ (Fig. S6, Supporting Information) for CO production after 1440 min measurement, probably due to the continuous consumption of protons with the generation of CH_4 in the first two cycles experiment.

The UV-vis absorption spectra presented that the Sc and So exhibited the similar light absorption edge at 382–385 nm with a band gap of 3.22–3.25 eV and the 4 h irradiation does not affect the light absorption of these materials (Fig. S7, Supporting Information). The density functional theory calculations suggested that the band structures of Sc and So were mainly composed of O2p valence band (VB) and Sn 5s conduction band (CB) (Fig. S8, Supporting Information). The flat band potentials of Sc and So were determined by Mott-Schottky curves to be -0.48 and -0.14 V vs. reversible hydrogen electrode (RHE), respectively (Fig. S9, Supporting Information), suggesting that the CB potentials for Sc and So were respectively -0.68 and -0.34 V vs. RHE. It means that CO_2 could be reduced to CO (-0.12 V vs. RHE) over Sc and So in terms of reaction thermodynamics. Correspondingly, the VB edges located at $+2.57$ V vs. RHE for Sc and $+2.88$ V vs. RHE for So are able to oxidize $-\text{OH}$ (1.23 V vs. RHE) adequately. Furthermore, the So and Sc share the nearly same specific surface area. The CO_2 adsorption on So is about 1.4 times higher than that on Sc (Fig. S10, Supporting Information), demonstrating that the CO_2 adsorption is dependent on the amount of terminal hydroxyls [23,33]. After 4 h pre-irradiation, the BET specific surface area and CO_2 adsorption quantity (Fig. S10, Supporting Information) both of Sc and So increased, illustrating that the FLPs generation could promote the adsorption of CO_2 molecule. Additionally, after FLPs generation, the CO_2 adsorption quantity of So (2.19 mg g^{-1}) was still higher than that of Sc (1.06 mg g^{-1}), confirming that the FLPs with short acid-base distance have the more strong capturing ability of CO_2 molecule.

3.4. Catalytic mechanism of FLPs

Based on the above results, we can conclude the CO_2 reduction mechanisms over Sc and So with different kinds of FLPs. As shown in Fig. 4a, first of all, under vacuum irradiation of Sc, O_{Vs} formed via photocorrosion of light-unstable Sn-OH terminal hydroxyls, and FLPs could be produced between O_{Vs} (Lewis acid) and its adjacent Zn-OH terminal hydroxyls (Lewis base) with a big space distance of 0.488 nm. Then H_2 was captured by FLPs, resulting in the heterolysis of H_2 and the formation of Zn-OH₂ and Sn-H species via protonation. Subsequently, the electrophilic C and nucleophilic O of CO_2 molecule prefer to interact with FLPs with high-activity protons, resulting in the generation of Sn-OH at Lewis acid sites through the insertion of oxygen from the breakage of C-O bond and the generation of Zn-OH₂-C=O species at Lewis base sites via the C atom of CO_2 binding to H of Zn-OH₂. Finally, Sn-OH was re-oxidized by h^+ to $^*\text{OH}$ to generate O_{Vs} (Lewis

acid) and the H in Zn-OH₂-C=O was reduced by electron to $^*\text{H}$ via $-\text{H}-\text{C}-$ bond breaking, thus releasing CO to regenerate Zn-OH (Lewis base) and combining $^*\text{OH}$ with $^*\text{H}$ to produce H_2O . For So, the similar CO_2 reduction route to Sc would occur. However, the obvious difference is that the FLPs on So have the smaller acid-base space distance of 0.207 nm, thus significantly accelerating the CO_2 reduction due to the strong orbital interactions (Fig. 4b). In addition, the CH_4 was detected as a minor product. Different from the CO yields, the CH_4 yields for samples with different pre-irradiation time have no obvious variation (Fig. S1, Supporting Information), independent on the O_{Vs} concentration or FLPs concentration. The results perhaps indicate that the CH_4 derived from the photoreduction reaction of $\text{CO}_2 + 2 \text{H}_2\text{O} \rightarrow \text{CH}_4 + 2 \text{O}_2$ without the help of FLPs.

3.5. The combination effects between facet junction and FLPs

Creating facet junction has been demonstrated to be an efficient route to enhance the charge separation [34,35]. It was well confirmed that, for $\text{ZnSn}(\text{OH})_6$, thermodynamically, the photoinduced electrons tend to transfer from (100) to (111) facets, while holes transfer in the opposite direction [33]. This conclusion inspires us to design $\text{ZnSn}(\text{OH})_6$ catalyst with the combination effects of FLPs activating CO_2 molecules and facet junction enhancing charge separation. As shown in Fig. 5a and b, the $\text{ZnSn}(\text{OH})_6$ cuboctahedra (denoted as Sco) with the coexposed (100) and (111) facets are the ideal material to achieve the combination effects of FLPs and facet junction. The (111) and (100) facets on Sco are the electron and hole accumulated facets, respectively, due to that both the CB and VB levels of (111) facet are slightly lower than those of (100) facet [33]. The junction electric field between (100) and (111) will drive directional charge drift, thus improving the charge separation efficiency. After 4 h vacuum irradiation, the EPR signals of O_{Vs} and protons trapped at O_{Vs} verified that the FLPs generation on Sco (Fig. 5c). And after CO_2 reduction the 1:3:3:1 EPR signal is a result of generation of $^*\text{CH}_3$ species [32], well indicating the interactions between FLPs and gaseous molecules (CO_2 and H_2). As expected, the CO and CH_4 yields on Sco were increased up to 11.75 and 1.43 $\mu\text{mol g}_{\text{cat}}^{-1} \text{h}^{-1}$ (Fig. 5d), evidently higher than those on Sc and So. The improved product generation rate would be attributed to the enhanced charge separation by facet junction electric field because the concentration of FLPs on the (100) and (111) facets of Sco is respectively similar to that on (100) facet of Sc and (111) facet of So. This evidence concededly supported a standpoint that combination of facet junction and FLPs is a potential route to enhance photochemical reaction kinetics.

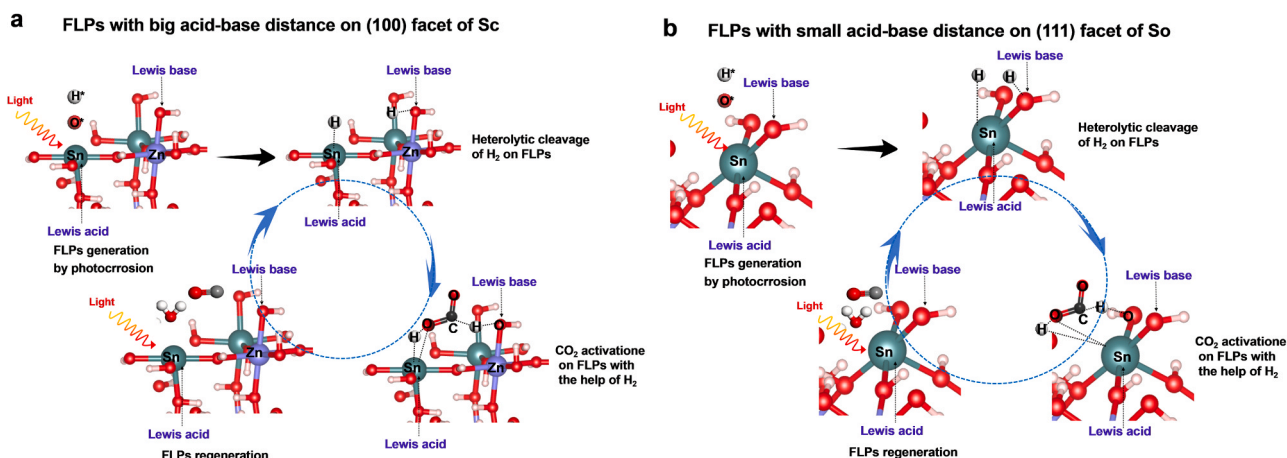


Fig. 4. CO_2 reduction mechanism over FLPs with big acid-base distance on (100) facet of Sc (a) and FLPs with small acid-base distance on (111) facet of So (b).

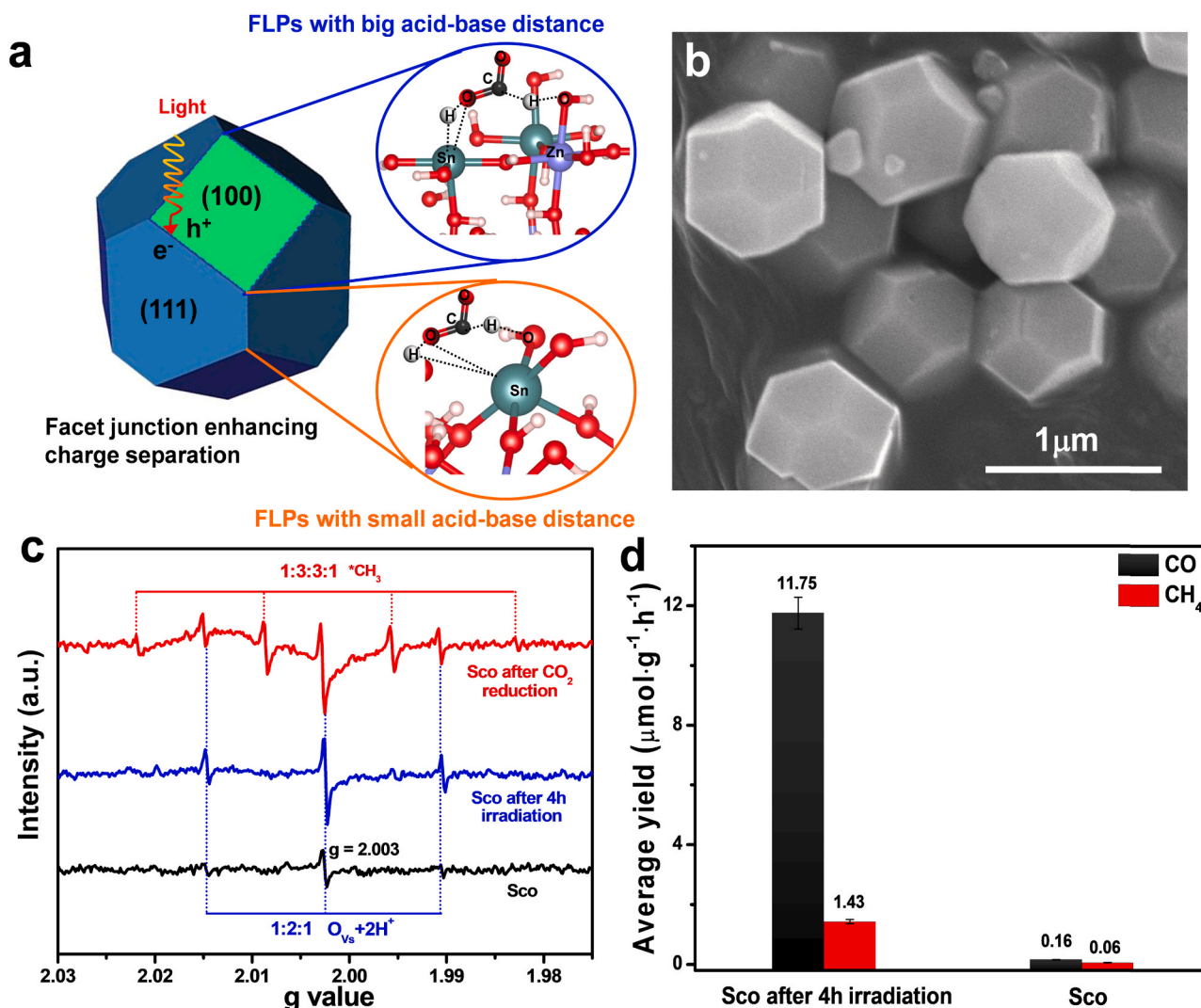


Fig. 5. (a) A scheme to describe the combination effects of facet junction enhancing charge separation and FLPs activating CO₂ molecules. (b) SEM image of single-crystal ZnSn(OH)₆ cuboctahedra. (c) EPR spectra. (d) CO and CH₄ yields.

4. Conclusions

In summary, by using vacuum irradiation, the FLPs with different acid-base distances were constructed on (100) facet of ZnSn(OH)₆ cube and on (111) facet of ZnSn(OH)₆ octahedra. The FLPs with short acid-base distance exhibited the more strong activation ability of molecules due to the strong orbital interactions, well demonstrating that designing of acid-base centers in FLPs is an efficient route to enhance the catalytic activity. We have demonstrated that the molecule catalysis by FLPs is able to couple with the facet junction electric field separating charge to enhance the photochemical energy conversion.

CRediT authorship contribution statement

The work was conceived and designed by Shicheng Yan; Weining Zhang, Zhenhua Yang and Hailian Wang fabricated the photocatalysts and performed the CO₂ reduction experiments; Depei Liu and Taozhu Li assisted in the fabrication of catalysts and spectroscopic measurements; Weining Zhang and Lei Lu drafted the manuscript and revised the manuscript; Shicheng Yan, Hao Qin and Tao Yu are in charge of data curation, funding acquisition, project administration and validation; and all authors discussed the results.

Declaration of Competing Interest

The authors declare that they have no known competing financial interests or personal relationships that could have appeared to influence the work reported in this paper.

Acknowledgements

This work was supported primarily by the National Natural Science Foundation of China (Grant Nos. 21633004, 21603098, 51572121, 51872135 and 51902137), the Fundamental Research Funds for the Central Universities (Grant Nos. 021314380084 and 021314380133), the Natural Science Foundation of Jiangsu Province (Grant Nos BK20151383, BK20150580 and BK20151265), the Postdoctoral Science Foundation of China (2020M671436) and the Postdoctoral Science Foundation of Jiangsu Province (2020Z022).

Appendix A. Supporting information

Supplementary data associated with this article can be found in the online version at [doi:10.1016/j.apcatb.2021.120748](https://doi.org/10.1016/j.apcatb.2021.120748).

References

- [1] C. Terrer, R.P. Phillips, B.A. Hungate, J. Rosende, J. Pett-Ridge, M.E. Craig, K. J. van Groenigen, T.F. Keenan, B.N. Sulman, B.D. Stocker, P.B. Reich, A.F. A. Pellegrini, E. Pendall, H. Zhang, R.D. Evans, Y. Carrillo, J.B. Fisher, K. Van Sundert, S. Vicca, R.B. Jackson, A trade-off between plant and soil carbon storage under elevated CO₂, *Nature* 591 (2021) 599–603.
- [2] A.M. Khenkin, I. Efremenko, L. Weiner, J.M. Martin, R. Neumann, Photochemical reduction of carbon dioxide catalyzed by a ruthenium-substituted polyoxometalate, *Chem. Eur. J.* 16 (2010) 1356–1364.
- [3] A. Sanna, M. Uibu, G. Caramanna, R. Kuusik, M.M. Maroto-Valer, A review of mineral carbonation technologies to sequester CO₂, *Chem. Soc. Rev.* 43 (2014) 8049–8080.
- [4] W.G. Tu, Y. Zhou, Z.G. Zou, Photocatalytic conversion of CO₂ into renewable hydrocarbon fuels: State-of-the-art accomplishment, challenges, and prospects, *Adv. Mater.* 26 (2014) 4607–4626.
- [5] K. Wang, J.L. Fu, Y. Zheng, Insights into photocatalytic CO₂ reduction on C₃N₄: Strategy of simultaneous B, K co-doping and enhancement by N vacancies, *Appl. Catal. B: Environ.* 254 (2019) 270–282.
- [6] H.N. Zhang, Y.F. Li, J.Z. Wang, N.N. Wu, H. Sheng, C.C. Chen, J.C. Zhao, An unprecedented hydride transfer pathway for selective photocatalytic reduction of CO₂ to formic acid on TiO₂, *Appl. Catal. B: Environ.* 284 (2021) 119692–119699.
- [7] L. Liu, N. Vankova, T. Heine, A kinetic study on the reduction of CO₂ by frustrated Lewis pairs: from understanding to rational design, *Phys. Chem. Chem. Phys.* 18 (2016) 3567–3574.
- [8] L. Liu, B. Lukose, B. Ensing, A free energy landscape of CO₂ capture by frustrated Lewis pairs, *ACS Catal.* 8 (2018) 3376–3381.
- [9] K.K. Ghuman, L.B. Hoch, T.E. Wood, C. Mims, C.V. Singh, G.A. Ozin, Surface analogues of molecular frustrated Lewis pairs in heterogeneous CO₂ hydrogenation catalysis, *ACS Catal.* 6 (2016) 5764–5770.
- [10] L.L. Liu, D.W. Stephan, Radicals derived from Lewis acid/base pairs, *Chem. Soc. Rev.* 48 (2019) 3454–3463.
- [11] D.J. Scott, M.J. Fuchter, A.E. Ashley, Designing effective ‘frustrated Lewis pair’ hydrogenation catalysts, *Chem. Soc. Rev.* 46 (2017) 5689–5700.
- [12] C.H. Lim, A.M. Holder, J.T. Hynes, C.B. Musgrave, Roles of the Lewis acid and base in the chemical reduction of CO₂ catalyzed by frustrated Lewis pairs, *Inorg. Chem.* 52 (2013) 10062–10066.
- [13] G.C. Welch, R.R. San Juan, J.D. Masuda, D.W. Stephan, Reversible, metal-free hydrogen activation, *Science* 314 (2006) 1124–1126.
- [14] Y.Y. Ma, S. Zhang, C.R. Chang, Z.Q. Huang, J.C. Ho, Y.Q. Qu, Semi-solid and solid frustrated Lewis pair catalysts, *Chem. Soc. Rev.* 47 (2018) 5541–5553.
- [15] S. Zhang, Z.M. Xia, Y. Zou, F.X. Cao, Y.X. Liu, Y.Y. Ma, Y.Q. Qu, Interfacial frustrated Lewis pairs of CeO₂ activate CO₂ for selective tandem transformation of olefins and CO₂ into cyclic carbonates, *J. Am. Chem. Soc.* 141 (2019) 11353–11357.
- [16] K.K. Ghuman, T.E. Wood, L.B. Hoch, C.A. Mims, G.A. Ozin, C.V. Singh, Illuminating CO₂ reduction on frustrated Lewis pair surfaces: investigating the role of surface hydroxides and oxygen vacancies on nanocrystalline In₂O_{3-x}(OH)_y, *Phys. Chem. Chem. Phys.* 17 (2015) 14623–14635.
- [17] T.J. Yan, L. Wang, Y. Liang, M. Makaremi, T.E. Wood, Y. Dai, B.B. Huang, A. A. Jelle, Y.C. Dong, G.A. Ozin, Polymorph selection towards photocatalytic gaseous CO₂ hydrogenation, *Nat. Commun.* 10 (2019) 2521–2530.
- [18] H.L. Wang, W.N. Zhang, L. Lu, D.P. Liu, D.D. Liu, T.Z. Li, S.C. Yan, S.Q. Zhao, Z. G. Zou, Dual-metal hydroxide with ordering frustrated Lewis pairs for photoactivating CO₂ to CO, *Appl. Catal. B: Environ.* 283 (2021) 119639–119645.
- [19] G. Kresse, J. Hafner, Ab initio molecular dynamics for liquid metals, *Phys. Rev. B* 47 (1993) 558–561.
- [20] G. Kresse, J. Hafner, Ab initio molecular dynamics for open-shell transition metals, *Phys. Rev. B* 48 (1993) 13115–13118.
- [21] J.P. Perdew, K. Burke, M. Ernzerhof, Generalized gradient approximation made simple, *Phys. Rev. Lett.* 77 (1996) 3865–3868.
- [22] H. Yan, Q. Shen, Y.H. Sun, S.M. Zhao, R.L. Lu, M.C. Gong, Y.B. Liu, X. Zhou, X. Jin, X. Feng, X.B. Chen, D. Chen, C.H. Yang, Tailoring facets of α-Mn₂O₃ microcrystalline catalysts for enhanced selective oxidation of glycerol to glycolic acid, *ACS Catal.* 11 (2021) 6371–6383.
- [23] S.M. Shu, C. Wang, S.T. Liu, Facile synthesis of perfect ZnSn(OH)₆ octahedral microcrystallines with controlled size and high sensing performance towards ethanol, *Front. Mater. Sci.* 12 (2018) 176–183.
- [24] H. Yu, R.Y. Lai, H.Q. Zhuang, Z.Z. Zhang, X.X. Wang, Controllable synthesis of crystallographic facet-oriented polyhedral ZnSn(OH)₆ microcrystals with assistance of a simple ion, *CrystEngComm* 14 (2012) 8530–8535.
- [25] Y.Y. Zhang, L.L. Wang, X.M. Ma, M.L. Yang, H.Y. Jiang, L. Li, C.C. Yuan, J.S. Shi, Amorphous carbon layer: An effective assistant for realizing near-infrared-activated photocatalysis, *J. Colloid Interf. Sci.* 531 (2018) 47–55.
- [26] R. Sahoo, A.K. Sasmal, C. Ray, S. Dutta, A. Pal, T. Pal, Suitable morphology makes CoSn(OH)₆ nanostructure a superior electrochemical pseudocapacitor, *ACS Appl. Mater. Interfaces* 8 (2016) 17987–17998.
- [27] S.L. Zhong, R. Xu, L. Wang, Y. Li, L.F. Zhang, CuSn(OH)₆ submicrospheres: Room-temperature synthesis, growth mechanism, and weak antiferromagnetic behavior, *Mater. Res. Bull.* 46 (2011) 2385–2391.
- [28] H.J. Yu, J.Y. Li, Y.H. Zhang, S.Q. Yang, K.L. Han, F. Dong, T.Y. Ma, H.W. Huang, Three-in-one oxygen vacancies: Whole visible-spectrum absorption, efficient charge separation, and surface site activation for robust CO₂ photoreduction, *Angew. Chem. Int. Ed.* 58 (2019) 3880–3884.
- [29] K.Y. Li, D.F. Xue, Estimation of electronegativity values of elements in different valence states, *J. Phys. Chem. A* 110 (2006) 11332–11337.
- [30] T.X. Wu, T. Lin, J.C. Zhao, H. Hidaka, N. Serpone, TiO₂-assisted photodegradation of dyes. 9. photooxidation of a squarylium cyanine dye in aqueous dispersions under visible light irradiation, *Environ. Sci. Technol.* 33 (1999) 1379–1387.
- [31] L.B. Knight, W. Weltner, Hyperfine interaction, chemical bonding, and isotope effect in ZnH, CdH, and HgH molecules, *J. Chem. Phys.* 55 (1971) 2061–2070.
- [32] L.O. Andersson, EPR investigation of the methyl radical, the hydrogen atom and carbon oxide radicals in Maxixe-type beryl, *Phys. Chem. Miner.* 35 (2008) 505–520.
- [33] L.Q. Tang, Z.Y. Zhao, Y. Zhou, B.H. Lv, P. Li, J.H. Ye, X.Y. Wang, M. Xiao, Z.G. Zou, Series of ZnSn(OH)₆ polyhedra: enhanced CO₂ dissociation activation and crystal facet-based homojunction boosting solar fuel synthesis, *Inorg. Chem.* 56 (2017) 5704–5709.
- [34] J.G. Yu, J.X. Low, W. Xiao, P. Zhou, M. Jaroniec, Enhanced photocatalytic CO₂-reduction activity of anatase TiO₂ by coexposed {001} and {101} facets, *J. Am. Chem. Soc.* 136 (2014) 8839–8842.
- [35] C.G. Zhou, J.K. Zhou, L. Lu, J.J. Wang, Z. Shi, B. Wang, L. Pei, S.C. Yan, Z.T. Yu, Z. G. Zou, Surface electric field driven directional charge separation on Ta₃N₅ cuboids enhancing photocatalytic solar energy conversion, *Appl. Catal. B: Environ.* 237 (2018) 742–752.